Physics of the Earth and Planetary Interiors 175 (2009) 167–182

Contents lists available at ScienceDirect

Physics of the Earth and Planetary Interiors

journal homepage: www.elsevier.com/locate/pepi

# Source process and tectonic implications of the 8 January 2006 ($M_w$ 6.7) Kythira earthquake, southern Greece

K.I. Konstantinou[a,*], S.-J. Lee[b], C.P. Evangelidis[c], N.S. Melis[c]

[a] Institute of Geophysics, National Central University, Jhongli, 320 Taiwan
[b] Institute of Earth Sciences, Academia Sinica, POB 1-55, Nankang, 115 Taiwan
[c] Institute of Geodynamics, National Observatory of Athens, POB 20048, 11810 Athens, Greece

ARTICLE INFO

*Article history:*
Received 17 June 2008
Received in revised form 12 March 2009
Accepted 13 March 2009

*Keywords:*
Relocation
Slip distribution
Moment rate function
Greece
Aegean
Kythira

ABSTRACT

On 8 January 2006 at 11:34 (GMT) a strong ($M_w$ 6.7) subcrustal earthquake occurred near Kythira island in southern Greece, causing damage to the surrounding area while the shock was also felt in most of the eastern Mediterranean. The event and its aftershocks were recorded by a regional network of 31 stations equipped with three-component broad-band seismometers that cover most parts of the Greek region. Initial locations of the earthquake sequence showed a diffuse pattern, therefore catalog and cross-correlation differential travel times were input to a shrinking grid-search relocation algorithm in order to obtain accurate relative locations. After this relocation most aftershocks form a tight cluster around the mainshock at depths between 44 and 53 km. Subsequently, waveforms from 12 stations giving the best possible azimuthal coverage around the Kythira event were inverted in order to investigate its source process. A parallel, non-negative least-squares inversion technique utilizing multiple time windows was used to derive the spatiotemporal slip distribution. The fault surface was parameterized by subfaults of 3 km × 3 km size covering a length and down-dip width of 91 and 100 km, respectively. Inversion results indicate that the fault plane is probably the one dipping towards SE. The slip distribution model showed that there are two areas of large slip (~60 cm), the largest extending between 38 and 80 km depth and a smaller one at depths 65–82 km. The moment rate function consists of a large initial peak with a duration of about 11 s followed by a number of smaller peaks, probably due to coseismic slip on some of the subfaults. Furthermore, the hypocenters of the relocated aftershocks coincide with the areas of minimum slip (<10 cm) while the hypocenter of the mainshock is located near the edge of the larger slip patch. Sensitivity and resolution tests confirmed the adequacy of the inversion parameters used and the stability of the solution. The Kythira earthquake was probably caused by the contortion of the downgoing African slab that results in the development of along-strike compression forces in the Kythira strait.



## 1. Introduction

The Hellenic subduction zone extends from the Ionian Sea in the west to the Aegean island of Rhodes in the east, exhibiting a strongly curved trench axis (Fig. 1). Its present day kinematics is manifested by the northward underthrusting of the African plate at a rate of less than 1 cm year$^{-1}$ beneath the Aegean microplate which moves towards SW at a rate of 3.5 cm year$^{-1}$ (e.g., McClusky et al., 2000; Nyst and Thatcher, 2004). Tomographic images have provided evidence about the shape and extent of the descending slab by inverting both teleseismic (Spakman et al., 1988) and regional (Papazachos and Nolet, 1997) travel time data. The results of these studies have clearly shown that the high-velocity anomaly associated with the slab extends to depths of up to 600 km and that its horizontal projection is asymmetric, with the western part being larger than the eastern one.

A direct consequence of the subduction process is the occurrence of intermediate-depth seismicity along the southern Aegean Sea, where a well defined Wadati–Benioff zone is formed. A series of studies have revealed that the Wadati–Benioff zone dips progressively towards NE reaching a maximum depth of 180 km in the eastern part of the subduction (Hatzfeld and Martin, 1992; Papazachos et al., 2000). Based on this hypocentral distribution it was also possible to infer an apparent difference in the dipping angles of the Wadati–Benioff zone between the shallow (20–100 km) part of the slab (~30°) and the deeper (100–180 km) one that dips at a steeper angle (~45°). Available focal mechanisms of intermediate-depth earthquakes display mostly down-dip extension in the eastern part of the subduction and along-strike compression in the western part (Hatzfeld et al., 1993; Kiratzi and Papazachos, 1995; Papazachos et al., 2000; Benetatos et al., 2004). This indicates a complicated slab deformation regime

* Corresponding author. Fax: +886 3 4222044.
*E-mail address:* kkonst@ncu.edu.tw (K.I. Konstantinou).

0031-9201/$ – see front matter © 2009 Elsevier B.V. All rights reserved.
doi:10.1016/j.pepi.2009.03.010

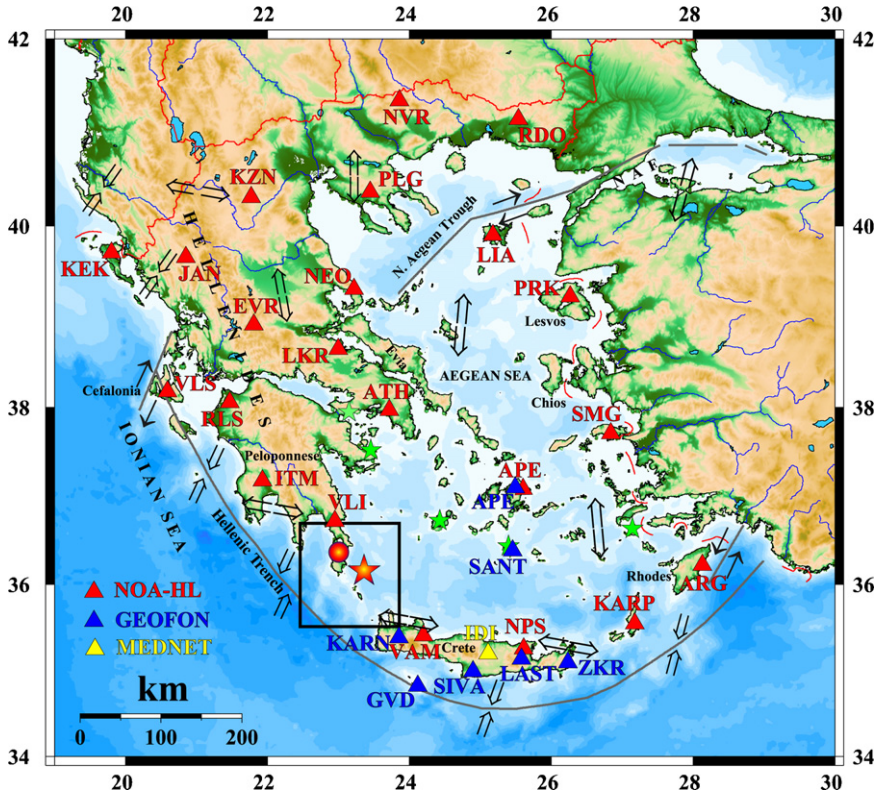


**Fig. 1.** Map showing the main tectonic features in the Greek region (after Papazachos and Papazachou (1997)) and locations of seismic stations (triangles) operated by NOAIG and other groups. The Hellenic trench and main faults are noted with thick black lines while arrows indicate the prevailing stress regime (compressional, extensional or strike-slip). Green stars represent active volcanic centers. The area inside the square is the Kythira strait where the 1903 (filled circle, location taken from Papazachos and Papazachou (1997)) and 2006 (filled star) earthquakes occurred. (For interpretation of the references to color in this figure legend, the reader is referred to the web version of the article.)

that is probably dominated by both slab-pull and compressional forces.

Even though most intermediate-depth earthquakes have relatively small local magnitudes (<4) and are barely felt, there are historical accounts as well as instrumental records of much larger events (for an overview see Papazachos and Papazachou, 1997). The macroseismic intensity field of such events is completely different from that of crustal earthquakes, in the sense that the former are usually felt in the convex part of the fore arc area (Peloponnese, Crete, central/western Greece), but not in the concave part which coincides with the back arc (northern Greece, NE Aegean). This characteristic can be explained by considering the fact that shear waves, responsible for much of the shaking caused during an earthquake, propagate efficiently within the cold, high-strength slab. However, shear waves are strongly attenuated as they travel through the partially molten mantle wedge (Konstantinou and Melis, 2008 and references therein). Ambraseys and Adams (1998) and Ambraseys (2001) give specific examples of the far-field effects of such earthquakes in the broader area of eastern Mediterranean.

The Kythira strait had been previously the focus of large intermediate-depth events, the strongest of which occurred in 1903 and caused extensive damage on the island of Kythira and in southern Peloponnese (Papazachos and Papazachou, 1997) (Fig. 1). On 8 January 2006, at 11:34:54 (hereafter all times are given in GMT) another strong event occurred offshore Kythira island, causing damage to buildings and landslides in a similar pattern to the 1903 earthquake. The first seismological results as well as a description of the observed macroseismic intensity field can be found in Konstantinou et al. (2006). This work uses regional waveform data in order to refine these earlier results and to elucidate the source characteristics of the latest Kythira event. Our analysis includes the precise relocation of the earthquake sequence and a finite fault inversion for estimating the slip distribution and rupture process of the mainshock. Finally, all these results are combined with previous knowledge of plate tectonics and velocity structure of the southern Aegean in an effort to interpret the occurrence of the Kythira earthquake.

## 2. Data

The Greek region is seismically monitored by the Hellenic broadband seismic network (HL) which is operated by the National Observatory of Athens, Institute of Geodynamics (hereafter called NOAIG) (Fig. 1). The HL network consists of 23 seismic stations that are equipped with three-component seismometers recording continuously at a sampling interval of 50 samples $s^{-1}$, while absolute timing is provided by GPS receivers. Most of the sensor types are Lennartz Le-3D (20 s) but there are also few Guralp CMG-40T (30 s) sensors. In addition to the HL stations there are also eight stations installed by the GEOFON and MEDNET groups equipped with three-component STS-2 seismometers which are operated in collaboration with NOAIG. All recorded signals are transferred via dedicated telephone lines in near real-time to a collection center in Athens where they are stored for analysis. Further information about seismic stations operation, data handling and quality check can be found in Melis and Konstantinou (2006) and in the dedicated web page of the HL network (http://bbnet.gein.noa.gr).

At the time of the occurrence of the Kythira earthquake all stations were operational, however, due to the strong ground motion several of them were saturated in one component (ITM, GVD) or more than one (VLI, VAM, KARN, SIVA, IDI). Arrival times of P- and S-phases were manually picked and were inverted using HYPO2000

**Table 1**
Velocity model derived from Papazachos and Nolet (1997) that was used for the initial and relative locations of the Kythira earthquake sequence.

| Depth (km) | P-wave velocity (km s$^{-1}$) |
|---|---|
| 19 | 6.00 |
| 31 | 6.60 |
| 50 | 7.90 |
| 100 | 7.95 |
| 120 | 8.00 |
| ∞ | 8.05 |

**Table 2**
Summary of source parameters and focal mechanism solutions reported by different agencies for the 8 January 2006 Kythira earthquake (ETH: Swiss Seismological Service, HRV: Harvard CMT, INGV: Italian National Institute of Geophysics and Volcanology, AUTH: Aristotle University of Thessaloniki, USGS: US Geological Survey).

| Agency | Lat | Lon | Depth (km) | $M_w$ | $M_0$ (dyn cm) | Strike | Dip | Rake |
|---|---|---|---|---|---|---|---|---|
| ETH | 36.29 | 23.24 | 55 | 6.8 | 1.73E+026 | 187 | 52 | 33 |
| HRV[a] | 35.81 | 23.28 | 61 | 6.7 | 1.51E+026 | 201 | 44 | 55 |
| INGV[a] | 35.97 | 23.42 | 79 | 6.7 | 1.40E+026 | 189 | 52 | 29 |
| AUTH | 36.16 | 23.36 | 64 | 6.7 | 1.30E+026 | 71 | 52 | 120 |
| USGS | 36.25 | 23.49 | 66 | 6.7 | 1.30E+026 | 193 | 43 | 59 |

[a] Centroid location and depth is reported.

(Klein, 2002) assuming a 1D velocity model and $V_P/V_S$ ratio of 1.78 derived from Papazachos and Nolet (1997) (Table 1). This procedure yielded an epicenter to the east of Kythira island (36.21°N, 23.42°E) at a hypocentral depth of 65 km with formal location errors not exceeding 4 km. The local magnitude was estimated by simulating the response of a Wood–Anderson seismograph for the unclipped waveforms following the procedure of Hutton and Boore (1987) and a value of 6.5 was obtained. The largest aftershock following the Kythira event occurred approximately 6 min later (11:40:59) having a local magnitude of 4.6, while the overall aftershock activity consisted of only 47 events ($M_L$ 4.2–2.8) in the period between 8 January to 27 May 2006. Table 2 summarizes the source parameters and focal mechanisms reported by different agencies for the Kythira earthquake.

## 3. Earthquake relocation

The aftershocks that followed were initially located in a similar way to the mainshock as described previously. This resulted in a linear distribution of epicenters orientated in a NE–SW direction having a total length of about 40 km and hypocentral depths between 40 and 60 km (Fig. 2). In order to obtain more precise locations of this earthquake sequence we used the *COMPLOC* package (Lin and Shearer, 2006) that applies a shrinking grid-search relocation algorithm using the source specific station term (SSST) method (Richards-Dinger and Shearer, 2000; Lin and Shearer, 2005). The method accepts as input the initial location of events and their corresponding travel times, calculates iteratively station corrections for each source-receiver pair and inverts for a new set of locations. These source specific station corrections are the weighted median of residuals at a given station from *N* nearby events. Differential travel times from waveform cross-correlation can be also included in the procedure allowing further constraints to be put on the inversion.

For the application of this relocation method to the Kythira earthquake sequence we included both catalog and differential travel times, while the same 1D velocity model mentioned before was used. Differential travel times were obtained after lowpass filtering the waveforms at 5 Hz and using a time window of 3 s around the P-phase and 4 s around the S-phase. In order to avoid ambiguities with the Pg/P*n* cross-over distance, we cross-correlate waveforms recorded at stations within an epicentral distance of 200 km. Relative location uncertainties are estimated using a bootstrap technique where random errors are added to the picks and each event is relocated 200 times (see Shearer, 1997; Evangelidis et al., 2008). This procedure will result in a cloud of locations for whose horizontal and vertical scatter can be used in order to estimate formal errors.

The map with the relocated earthquake sequence consisting of a total of 48 events can be seen in the inset of Fig. 2 while depth cross-sections comparing the initial and relocated hypocenters can be found in Fig. 3. The Kythira mainshock has a relocated hypocentral depth of 51 km. Most of the aftershocks appear to be located at similar depths (44–53 km) around the mainshock, forming a tight

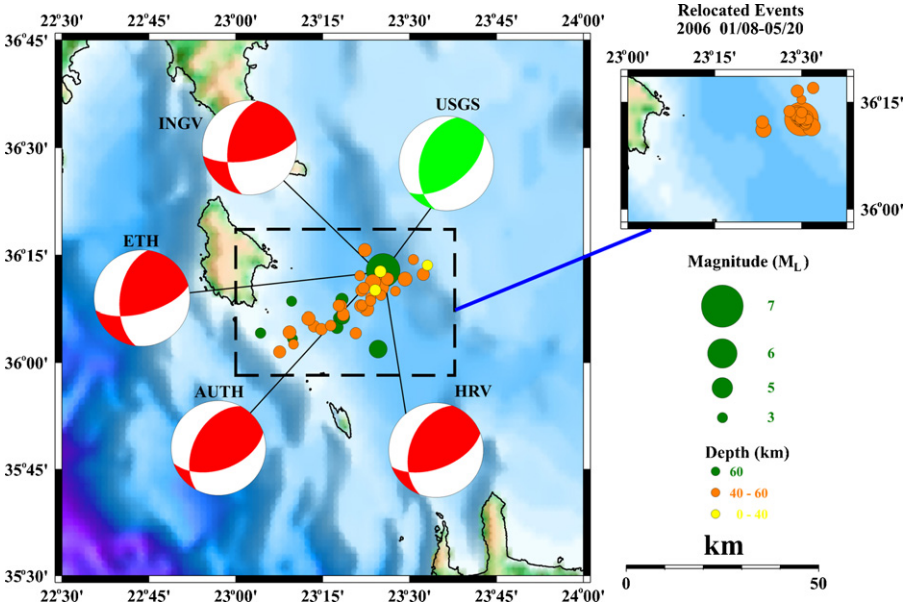


**Fig. 2.** Map showing the distribution of epicenters for the mainshock of the Kythira earthquake and its aftershocks. The circle size/color is proportional to the local magnitude/depth of each event according to the scales shown at the right of the plot. Focal mechanism solutions for the mainshock are also plotted (see Table 2 for more details). The inset at the right hand corner of the plot is proportional to the dashed square on the main map and shows the relocated earthquake sequence (see text for more details). (For interpretation of the references to color in this figure legend, the reader is referred to the web version of the article.)

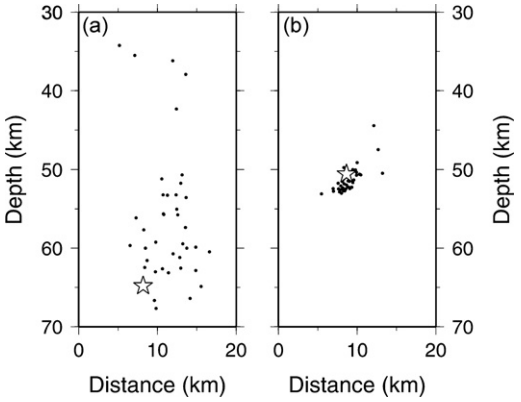


**Fig. 3.** Depth cross-sections along a NW–SE direction of (a) the initial locations of the mainshock–aftershock sequence using HYPO2000, and (b) the relative locations calculated using the shrinking grid-search algorithm. The star represents the Kythira earthquake hypocenter.

cluster around it. The quality of this relocation can be assessed by jointly considering: (a) the distribution of cross-correlation values for the P- and S-phases between event pairs which have a peak in the range 0.70–0.80 (Fig. 4a), (b) the number of stations where the cross-correlation value is higher than 0.55 and in our case this happens at four or more stations (mostly VLI, GVD, SANT, SIVA, ITM) (Fig. 4b and c), (c) the results of the bootstrap error estimation, showing that both the horizontal and vertical errors for all events are smaller than 1 km. It should be noted that cross-correlation values for P- seem to be somewhat higher than the S-phases. This is probably because the coda of the P-phase interferes with the onset of the S, lowering its correlation value between stations. Comparing the initial locations with the relocated ones, we see that the former appear elongated along the NE–SW direction which also coincides with the direction where there is a gap in the station azimuthal distribution. The catalog of the relocated events along with their bootstrap error estimates can be found in Table 3.

## 4. Finite fault inversion

### 4.1. Method and rationale

The theoretical background of any finite fault inversion problem has as a starting point the parameterization of the fault surface in a number of sufficiently smaller area subfaults. The recorded ground motion can then be represented as a sum of the products of the Green's functions and the slip that occurred on each of these subfaults (Lay and Wallace, 1995). This can be further recast in the well-known linearized form, $\mathbf{Ax} = \mathbf{b}$ where **A** is the matrix of the Green's functions, **x** is the solution vector of slip on each subfault and **b** is the observed data vector (Fig. 5). The system of equations can be solved by standard least-squares methods, but sometimes the problem may become unstable and it is necessary to add linear stability constraints such as smoothing, damping and moment minimization. This methodology was successfully used in a series of finite fault inversion studies of many large earthquakes worldwide (e.g., Hartzell and Heaton, 1983; Lee and Ma, 2000; Ma et al., 2001, among others).

An important improvement to the methodology described above is the introduction of multiple-time windows in the inversion problem, resulting in a better spatiotemporal resolution of slip. This is accomplished first by forming the columns of matrix **A** as the Green's functions strung end to end for each subfault and for all the stations in the inversion. In a similar way matrix **b** is formed by stringing all observation records end to end. Subsequently, matrix **A** is rearranged by taking *Nt* time windows and putting them side

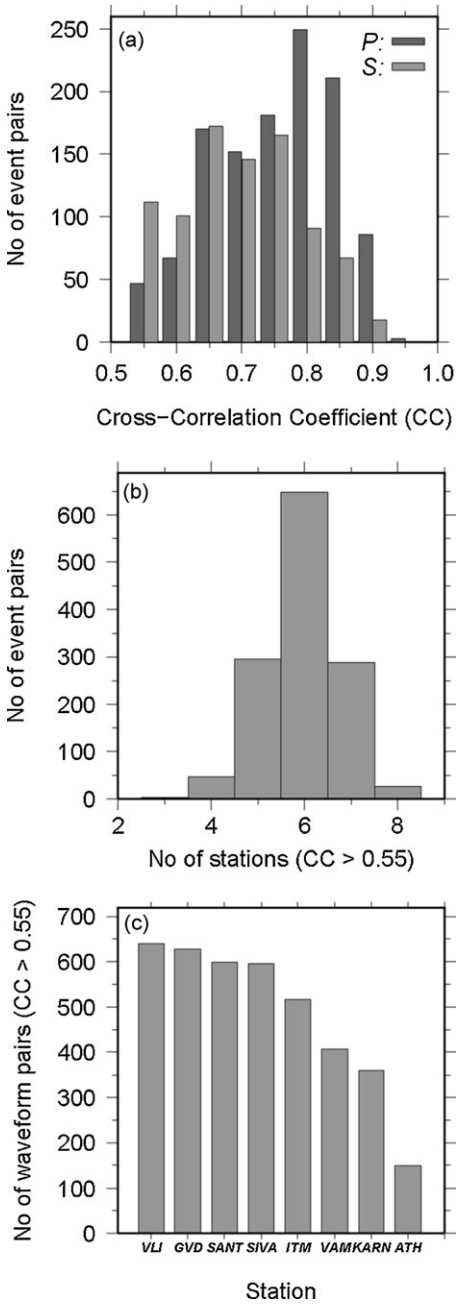


**Fig. 4.** (a) Histogram of the distribution of cross-correlation coefficients for P- and S-phases respectively, (b) distribution of the number of stations that had a cross-correlation coefficient higher than 0.55, and (c) distribution of the number of waveform pairs with cross-correlation coefficient higher than 0.55 at stations used in the relocation.

by side, while vector **x** becomes *Nt* times the single time window where *Nt* is the number of windows (Fig. 5). An increase in the number of time windows would lead to a large expansion of matrix **A** making the solution of this problem very costly in terms of computer time. Program performance can be improved by applying a parallel non-negative least-squares (NNLS) inversion technique which decomposes matrix **A** into different computing nodes and solves for the vector **x** for each time window. All slip on the fault must be initiated after the rupture front has passed through, so that the source duration time starts counting after this rupture delay time. In our multiple-time window analysis, each subfault is allowed to slip in any of the 2 s time windows following the passage of the rupture front while each window may have an overlap

**Table 3**
Summarizing the results of the relocation procedure for the Kythira event and its 47 aftershocks.

| O.T. | Lat | Lon | Depth (km) | Err*H* | Err*V* | $M_L$ |
|---|---|---|---|---|---|---|
| 060108113454 | 36.21066 | 23.49988 | 50.571 | 0.89 | 0.63 | 6.5 |
| 060108114059 | 36.19230 | 23.52865 | 53.090 | 0.45 | 0.44 | 4.6 |
| 060108114717 | 36.21542 | 23.49463 | 50.234 | 0.67 | 0.53 | 3.9 |
| 060108120627 | 36.20986 | 23.50456 | 51.189 | 0.77 | 0.52 | 3.5 |
| 060108122046 | 36.20633 | 23.49639 | 52.732 | 0.72 | 0.57 | 3.5 |
| 060108125105 | 36.20732 | 23.50101 | 49.764 | 0.77 | 0.49 | 3.6 |
| 060108132132 | 36.21722 | 23.50356 | 51.493 | 0.64 | 0.49 | 2.8 |
| 060108133213 | 36.21826 | 23.50387 | 52.291 | 0.82 | 0.56 | 3.0 |
| 060108171206 | 36.21827 | 23.49717 | 51.685 | 0.61 | 0.48 | 3.5 |
| 060108172356 | 36.22066 | 23.49313 | 50.730 | 0.58 | 0.44 | 3.7 |
| 060108173024 | 36.21855 | 23.48761 | 49.135 | 0.63 | 0.26 | 3.6 |
| 060108193953 | 36.20699 | 23.50202 | 51.028 | 0.71 | 0.50 | 3.0 |
| 060108195712 | 36.21140 | 23.51036 | 51.563 | 0.63 | 0.43 | 2.8 |
| 060109003752 | 36.20741 | 23.50338 | 52.351 | 0.73 | 0.42 | 2.8 |
| 060109053451 | 36.21365 | 23.48994 | 49.998 | 0.69 | 0.45 | 3.7 |
| 060109081310 | 36.21827 | 23.50508 | 51.088 | 0.92 | 0.49 | 3.6 |
| 060109091706 | 36.20844 | 23.50766 | 53.007 | 0.65 | 0.42 | 3.6 |
| 060109121447 | 36.21795 | 23.50412 | 52.449 | 0.80 | 0.56 | 3.4 |
| 060109155959 | 36.21737 | 23.50548 | 50.712 | 0.67 | 0.53 | 3.0 |
| 060109231111 | 36.22210 | 23.49753 | 50.043 | 0.67 | 0.43 | 3.3 |
| 060110223101 | 36.21206 | 23.50484 | 50.845 | 0.81 | 0.42 | 3.4 |
| 060111103450 | 36.22308 | 23.48683 | 50.698 | 0.85 | 0.57 | 4.3 |
| 060111182943 | 36.21988 | 23.50256 | 52.272 | 0.59 | 0.47 | 3.6 |
| 060111201402 | 36.21512 | 23.51273 | 51.844 | 0.68 | 0.51 | 3.8 |
| 060112022835 | 36.19865 | 23.51152 | 52.430 | 0.73 | 0.57 | 3.4 |
| 060113001612 | 36.21730 | 23.51038 | 51.973 | 0.62 | 0.47 | 2.9 |
| 060113151812 | 36.21242 | 23.50053 | 50.665 | 0.58 | 0.41 | 3.5 |
| 060116123722 | 36.21192 | 23.50346 | 52.495 | 0.67 | 0.46 | 3.0 |
| 060117112716 | 36.21280 | 23.51060 | 52.711 | 0.89 | 0.51 | 2.8 |
| 060118214349 | 36.20544 | 23.50485 | 52.072 | 0.71 | 0.45 | 3.1 |
| 060119172320 | 36.20918 | 23.49353 | 51.453 | 0.74 | 0.53 | 3.1 |
| 060121070327 | 36.20507 | 23.50747 | 52.866 | 0.73 | 0.53 | 3.1 |
| 060128191543 | 36.20715 | 23.50631 | 52.551 | 0.69 | 0.53 | 3.0 |
| 060129113705 | 36.19984 | 23.51263 | 52.767 | 0.82 | 0.55 | 2.9 |
| 060211055143 | 36.21650 | 23.49204 | 51.334 | 0.72 | 0.59 | 3.5 |
| 060215104118 | 36.18590 | 23.39020 | 46.030 | 0.00 | 0.00 | 4.2 |
| 060226042949 | 36.25600 | 23.49940 | 47.467 | 0.00 | 0.00 | 2.7 |
| 060314052018 | 36.20682 | 23.51224 | 52.453 | 0.67 | 0.46 | 2.9 |
| 060316070540 | 36.20971 | 23.51776 | 51.742 | 0.67 | 0.57 | 3.1 |
| 060404154120 | 36.22215 | 23.48817 | 50.621 | 1.03 | 0.86 | 3.9 |
| 060409203259 | 36.21105 | 23.49701 | 52.230 | 0.68 | 0.42 | 3.2 |
| 060419073017 | 36.28325 | 23.53318 | 50.496 | 0.00 | 0.00 | 3.4 |
| 060429225825 | 36.22876 | 23.46562 | 44.438 | 0.00 | 0.00 | 3.4 |
| 060511014747 | 36.34820 | 23.71870 | 52.990 | 0.00 | 0.00 | 3.9 |
| 060520010733 | 36.22551 | 23.50051 | 50.343 | 1.16 | 0.83 | 3.2 |
| 060524113121 | 36.27570 | 23.48810 | 56.510 | 0.00 | 0.00 | 3.6 |
| 060527032909 | 36.20370 | 23.38710 | 58.590 | 0.00 | 0.00 | 3.6 |

O.T. denotes the origin time of each event (GMT), Lat and Lon denote the latitudes and longitudes of the relocated epicenter and Err*H*, Err*V* denote the horizontal and vertical relocation errors, respectively.

of 1 s. If the slip occurs at a later time window its characteristic rupture delay time will be longer, therefore the rupture velocity will be relatively slow. Further information about this method and its application to finite fault inversion for the rupture process of the 1999 Chi-Chi, Taiwan earthquake can be found in Lee et al. (2006).

An alternative approach to the method described previously would be to use a smaller event as an empirical Green's function (EGF), estimate relative source time functions for the larger event and invert them for the slip distribution (e.g., Dreger, 1994). Obviously, the advantage of such an approach is that calculation of theoretical Green's functions using an inaccurate velocity model is avoided. Necessary conditions for this scheme to work is that the smaller event can be treated as a point source, it has a similar focal mechanism and is located close enough to the larger event. We tried to identify suitable EGF events for such an analysis from the aftershocks that were clustered close to the Kythira earthquake hypocenter. However, most of them had local magnitudes smaller than 4 and their signal-to-noise ratio deteriorated significantly to the more distant stations. Initial deconvolution tests did not yield satisfactory results, therefore we opted for using the NNLS multiple time window method instead.

**Table 4**
Velocity model used to calculate Green's functions.

| Depth (km) | P-wave velocity (km s$^{-1}$) |
|---|---|
| For paths traversing the southern Aegean (Karagianni et al., 2005) | |
| 2.50 | 2.97 |
| 14.50 | 5.87 |
| 20.50 | 5.96 |
| 27.50 | 7.65 |
| 34 | 6.62 |
| 80 | 7.25 |
| 120 | 8.00 |
| ∞ | 8.05 |
| For paths traversing the Peloponnese (Novotny et al., 2001) | |
| 1 | 2.31 |
| 2 | 4.27 |
| 5 | 5.52 |
| 16 | 6.23 |
| 33 | 6.41 |
| 59 | 7.60 |
| 100 | 7.95 |
| ∞ | 8.00 |

### 4.2. Slip distribution models and preferred solution

The selection of stations in the inversion process is mainly related to the uncertainties concerning the available 1D velocity models that would account for propagation effects. In order to minimize these uncertainties but at the same time maximize the azimuthal coverage, we chose to include stations with epicentral distances not larger than 250 km. Another criterion is of course the quality of the recorded waveforms in terms of signal-to-noise ratio and possible saturation effects. As stated earlier stations GVD and ITM had each of them one component clipped, however, it was possible to include the other two components in the inversions. Also, in station APE two types of sensors are installed (Le-3D and STS-2) and the waveforms recorded by the STS-2 sensor were used. In this way, 34 recorded waveforms from 12 stations were selected that spanned an azimuthal coverage of about 212°, leaving a gap only at the SW direction towards the Mediterranean Sea.

Prior to the inversion the instrument response was removed from the recorded signals and the waveforms were filtered between 0.05–0.1 Hz using a four-pole Butterworth filter. Green's functions were calculated by the frequency–wavenumber method, using two velocity models: one for paths that traverse the southern Aegean Sea (Karagianni et al., 2005) and the other for paths that pass through the Peloponnese and western Greece (Novotny et al., 2001) (Table 4). Both of these models were derived from surface wave dispersion analysis and their depth resolution does not exceed 40–50 km. Therefore upper-mantle velocities were constrained using published values from the tomographic study of the Aegean region by Papazachos and Nolet (1997). Once the Green's functions were computed they were filtered between 0.05 and 0.1 Hz in the same way as the observed data.

The fault was parameterized by subfaults each having a dimension of 3 km × 3 km covering an area of length and down-dip width of 91 and 100 km, respectively. These values of length and down-dip width were chosen for the purpose of avoiding any underestimation of the true fault plane. In order not to exclude the possibility of supersonic rupture velocities, the starting value of rupture velocity was set to 10 km s$^{-1}$ but later rupture velocities in the inversion could vary between 0 and 10 km s$^{-1}$. We also chose to apply the NNLS method using 24 multiple time windows. Finally, we imposed some stability constraints such as minimization of the seismic

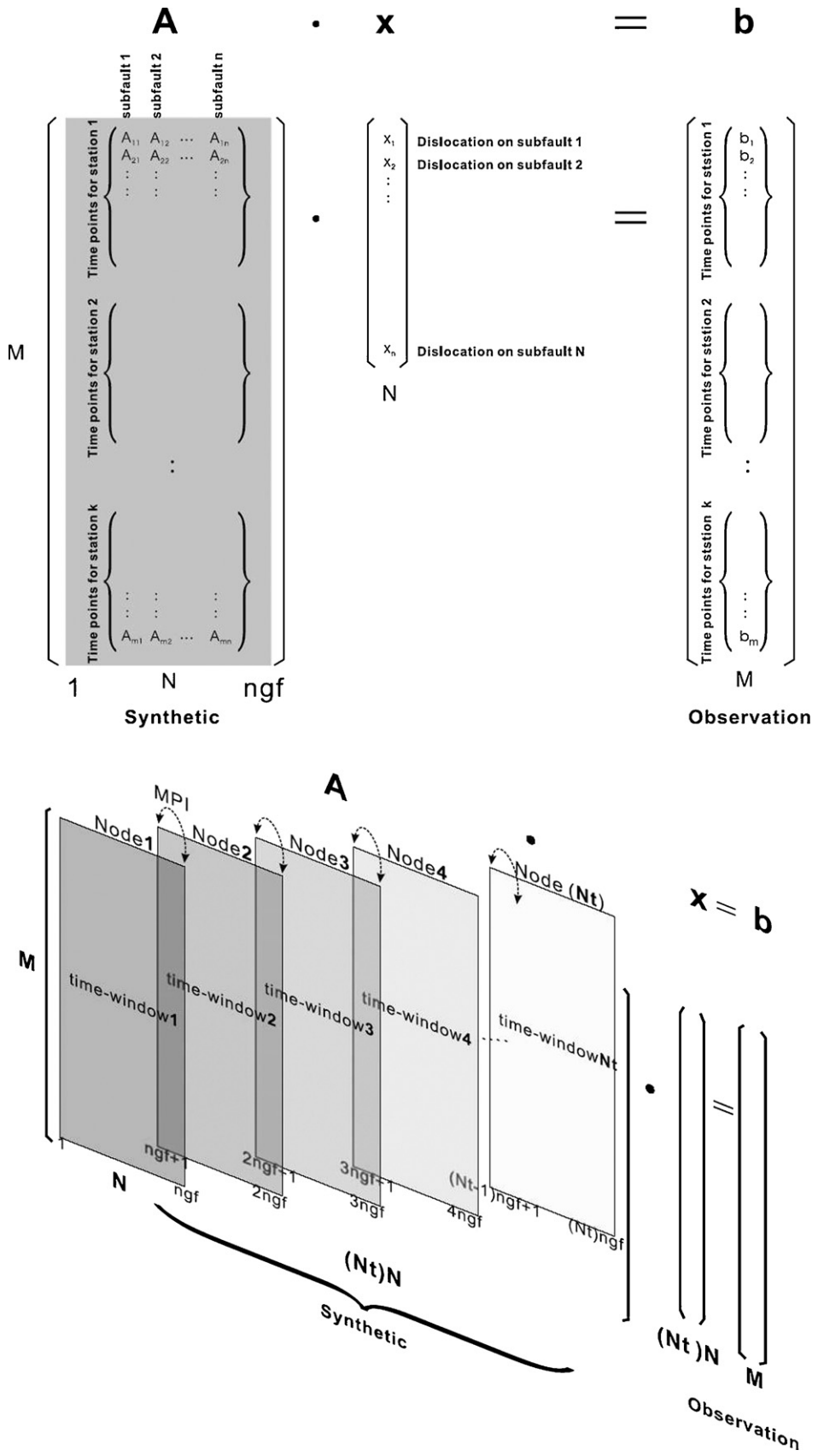


**Fig. 5.** Upper panel: traditional single time window matrix system used by previous studies to solve for the slip distribution along a fault (see text for details); lower panel: multiple time window approach where the matrix **A** is decomposed in the parallel NNLS inversion. Message passing interface (MPI) is applied as the communicant between the computing nodes in the parallel computing process (from Lee et al. (2006)).

moment and damping at the edge of the parameterized fault in order to avoid unrealistic slip distributions.

Several agencies reported moment tensor solutions for the Kythira event, some of them just a few minutes after its occurrence. These solutions can be grouped in two types based on their sense of motion: the first type (Harvard CMT, ETH, INGV, AUTH) represents reverse faulting with a substantial amount of strike-slip motion while the second one (USGS) exhibits again reverse faulting with almost no strike-slip component (see Fig. 2 and Table 1). Both groups seem to consistently have nodal planes orientated obliquely or perpendicular to the trench axis. A set of slip inversions was performed in order to investigate the effect of the focal mechanism solution on the slip distribution pattern. Fig. 6a shows the results of the slip inversions considering each time a different solution and testing both nodal planes, while the rupture initiation point on the fault was set to the relocated mainshock depth (51 km). It can be seen that for all solutions the misfit for the nodal planes dipping to the SE exhibit a smaller misfit, but more importantly the relocated events lie within regions of low slip unlike the case of the NW-dipping planes. Also, the slip distributions corresponding to the SE-dipping planes have fewer irregular, low-amplitude patches that are likely to be artifacts created by unmodeled propagation effects. Next we varied the rupture initiation point to the depth given by the initial HYPO2000 location (65 km) and repeated the slip inversions. The results showed that for all moment tensor solutions and for both nodal planes the misfit becomes significantly larger, indicating that the data are better fit by a shallower rather than a deeper source (Fig. 6b).

Based on these results we choose as our preferred slip distribution model the one that corresponds to the ETH moment tensor solution, since its reported hypocenter (55 km) is closer to the relocated depth and its misfit value is not considerably different from the others. This slip distribution model defines a rupture area of approximately 66 km in length and 50 km in down-dip width (Fig. 7). It consists of two patches of large slip (~60 cm) one extending between depths 38–80 km and a smaller but deeper patch that extends to depths 65–82 km. The relocated aftershock hypocenters have been also plotted in Fig. 7 and most of them are located in the area between the two patches which exhibits only a small amount of slip (<10 cm). This clustering of aftershocks at the one end of the rupture where a high slip gradient exists, is consistent with the suggestion that the largest stress increase is concentrated at the ends of the mainshock rupture (Das and Henry, 2003). The derived moment rate function shows that the largest amount of moment was released during the first 11 s however, there is also some moment release after that time, probably as a result of coseismic slip on the surface of the fault. This can be seen more clearly in Fig. 8 where snapshots of the rupture process as a function of time and space are shown. The two slip patches form almost at the same time (~6 s), while after the first 12 s the slip distribution pattern changes very little. The snapshots also provide an indication about the directivity of the rupture which seems to be unilateral towards the west.

### 4.3. Sensitivity and resolution tests

We performed several tests for the purpose of ascertaining the robustness of the features present in our preferred slip model. The first test had to do with investigating the dependence of the solution to the selected frequency band. The waveform data and Green's functions were filtered in two other frequency bands (0.05–0.125 Hz, 0.05–0.15 Hz) and inverted for the slip distribution as previously. The comparison between these results and the preferred slip model shows that in the band 0.05–0.125 Hz the slip distribution maintains its general characteristics, such as number/depth of asperities and their amplitude, however, their shape is altered (Fig. 9). Furthermore, as the upper cut-off frequency increases to 0.15 Hz the amplitude of the slip shifts to lower values for both patches. This indicates that our slip model is relatively stable only up to frequencies 0.125 Hz, a result not surprising if one considers that propagation effects were accounted for by using average 1D velocity models. At this point it should be noted that the moment release in our preferred model does not start at zero seconds, but there seems to be a gap of 2–3 s before it starts to grow. This gap begins to fill once we invert the data using a higher cut-off frequency, indicating that the initial rupture of the Kythira earthquake is probably enriched in higher frequencies.

In the next test we checked how the choice in the number of time windows affects our preferred slip distribution model. The data were inverted using 6, 12, 18 and 30 time windows and these inversion results were compared to our preferred model where 24 time windows had been used (Fig. 10). It can be seen that as the number of time windows increases, the overall waveform fit is improving while the slip distribution pattern remains essentially the same. Indeed, slip distributions that correspond to 18, 24 or 30 time windows exhibit minor differences and their misfits are very similar. The increase in the number of time windows has also the effect of prolonging the duration of the moment release from about 12 s in the case of 6 time windows, to 32 s if we use 30 time windows. Such a prolongation can be explained if we consider that by increasing the number of time windows we essentially view a larger portion of the temporal evolution of the rupture process.

The number of available stations and their distribution around the fault plane also plays an important role when trying to resolve slip characteristics. We examined the stability of the preferred slip model when a number of stations were removed each time and the results are shown in Fig. 11. Very little change is observed if we remove stations ITM (closest station to the epicenter) and RLS and invert only 29 out of the 34 available waveforms. The slip distribution does not change significantly either when the waveform number is further reduced to 20, even though the deeper patch becomes connected with the larger shallower patch. However, the solution starts to be altered when we try to invert only 14 waveforms and the amplitude of the slip patches shifts to lower values.

Finally, we performed a synthetic test where we tried to resolve "a priori" slip patches that vary in dimension, amplitude and depth, using three different subfault dimensions (3 km × 3 km, 4 km × 4 km, 5 km × 5 km). The synthetic slip model consisted of three patches, the smallest of them having a dimension of 15 km × 15 km while the lowest amplitude considered was of the order of 20 cm (Fig. 12). Synthetic waveforms were computed for each of our stations using forward modeling and these were subsequently inverted in the same way as in our preferred slip model (i.e., frequency band 0.05–0.1 Hz, 24 time windows, ETH moment tensor solution, 51 km hypocentral depth). The results show that the patches are well resolved both in the case of the 3 km × 3 km and 4 km × 4 km subfault dimensions, while resolution deteriorates significantly when the dimension becomes 5 km × 5 km.

## 5. Seismotectonic interpretation

Current knowledge about the plate configuration in the southern Aegean comes mainly from the delineation of the Wadati–Benioff zone (Papazachos et al., 2000), travel time tomography (Papazachos and Nolet, 1997) and more recently by receiver function analysis (Knapmeyer and Harjes, 2000; Li et al., 2003; Endrun et al., 2004; Sodoudi et al., 2006). The latter studies were found more efficient in detecting velocity discontinuities, such as the Moho and the Lithosphere–Asthenosphere Boundary (LAB) of the Aegean and African plates. The study of Sodoudi et al. (2006) covered most of the Greek region and revealed the following slab geometry characteristics: (a) a progressive deepening of the Moho depth from

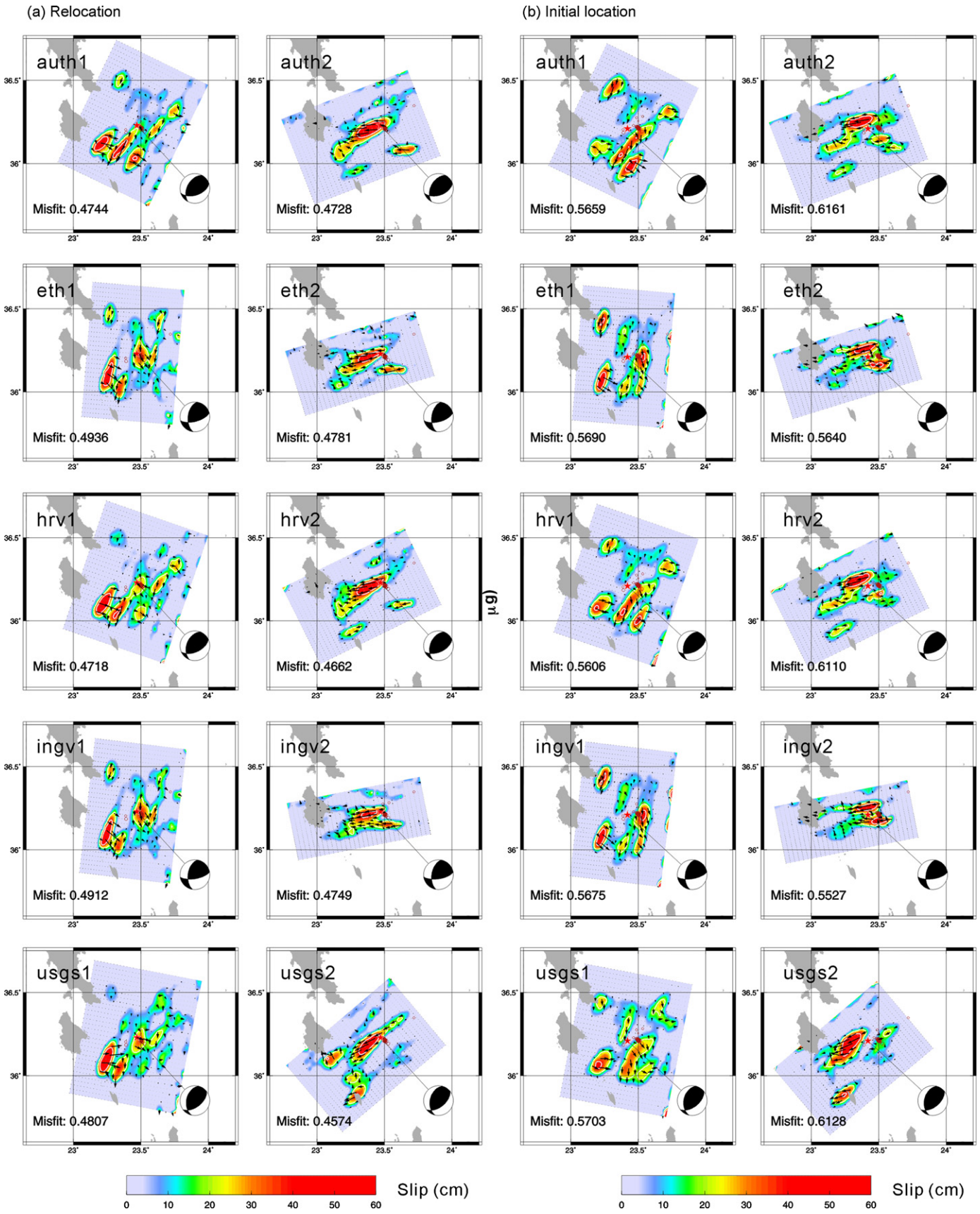


**Fig. 6.** Slip inversion results of the Kythira earthquake for focal mechanism solutions and their nodal planes reported by different agencies (see also Table 2) using (a) the relocated mainshock hypocenter (51 km) and (b) the hypocenter stemming from the initial location with HYPO2000 (65 km). Slip values vary according to the color scale shown at the bottom of the figure. Black arrows indicate the sense of slip motion on the surface of the fault. The star indicates the hypocenter of the mainshock and red circles the relocated aftershocks. The number after the name of each agency corresponds to nodal plane 1 or 2. (For interpretation of the references to color in this figure legend, the reader is referred to the web version of the article.)

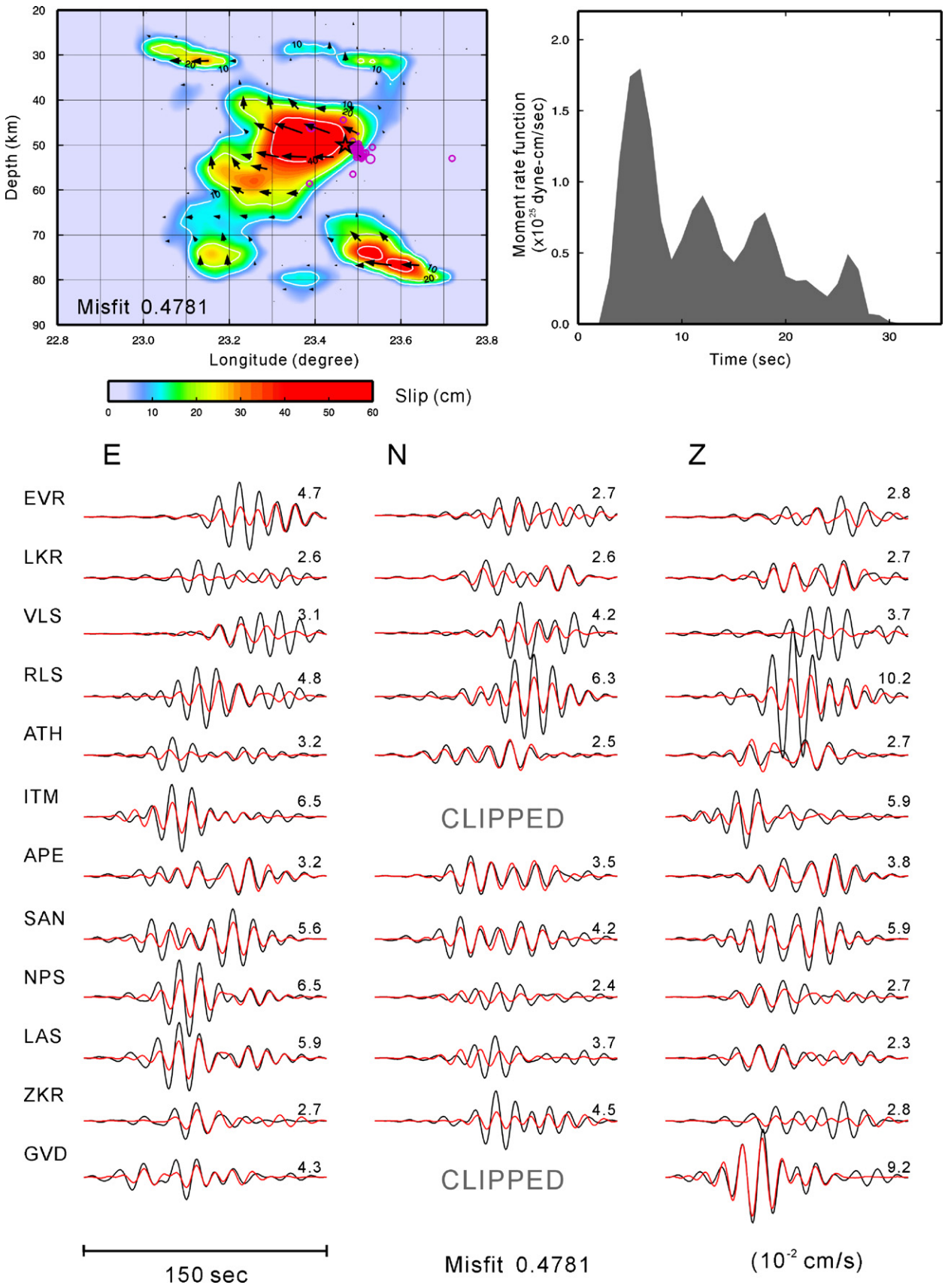


**Fig. 7.** Slip distribution and observed (black curves) versus synthetic (red curves) waveforms of the preferred inversion solution using the ETH focal mechanism solution. Symbols plotted are the same as in Fig. 6. The number at the right of each waveform represents the maximum amplitude of the observed seismogram. The moment rate function can be seen at the top right of the plot. (For interpretation of the references to color in this figure legend, the reader is referred to the web version of the article.)

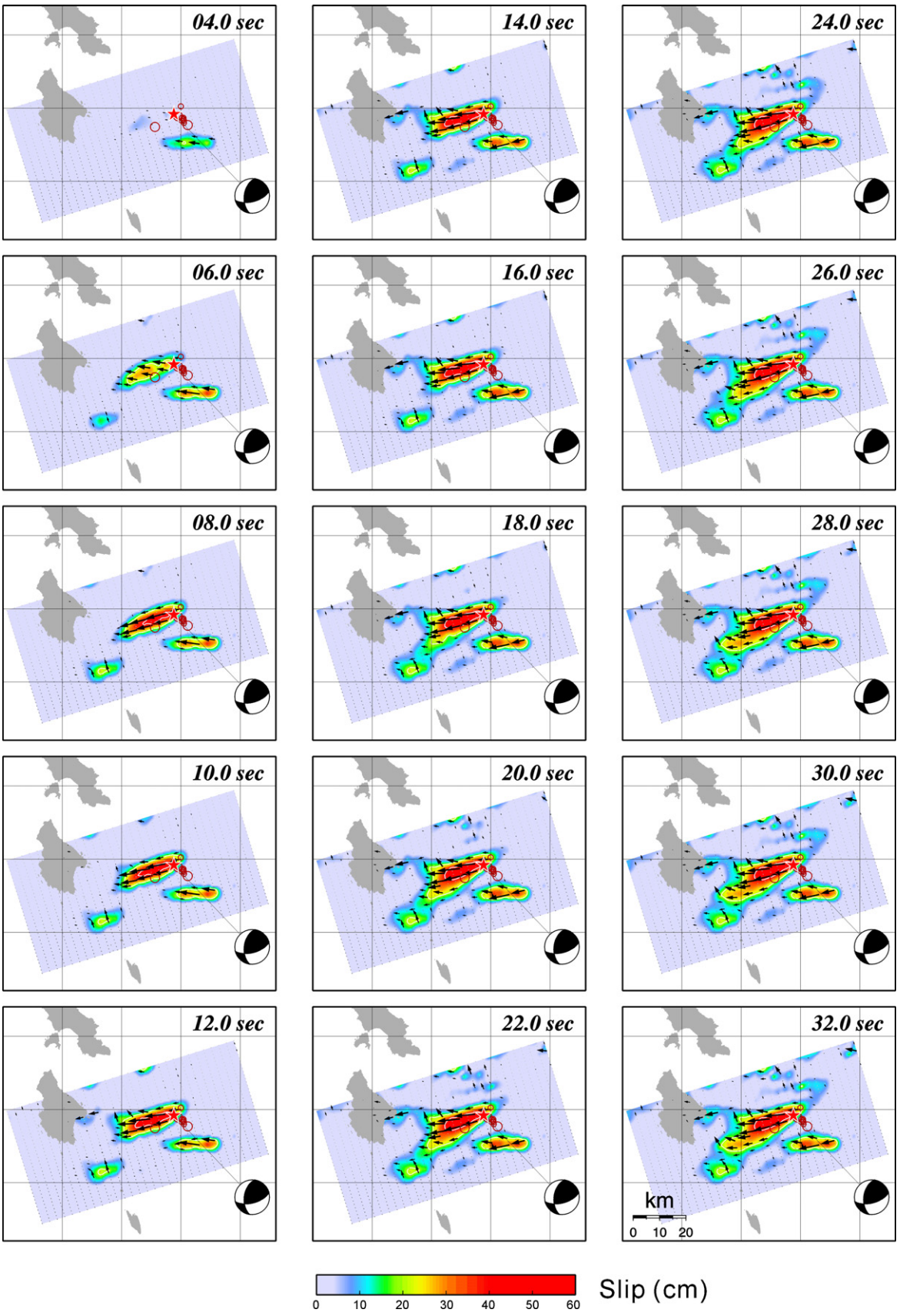


**Fig. 8.** Snapshots of the rupture process of the Kythira earthquake depicted every 2 s. Symbols plotted are the same as in Fig. 6.

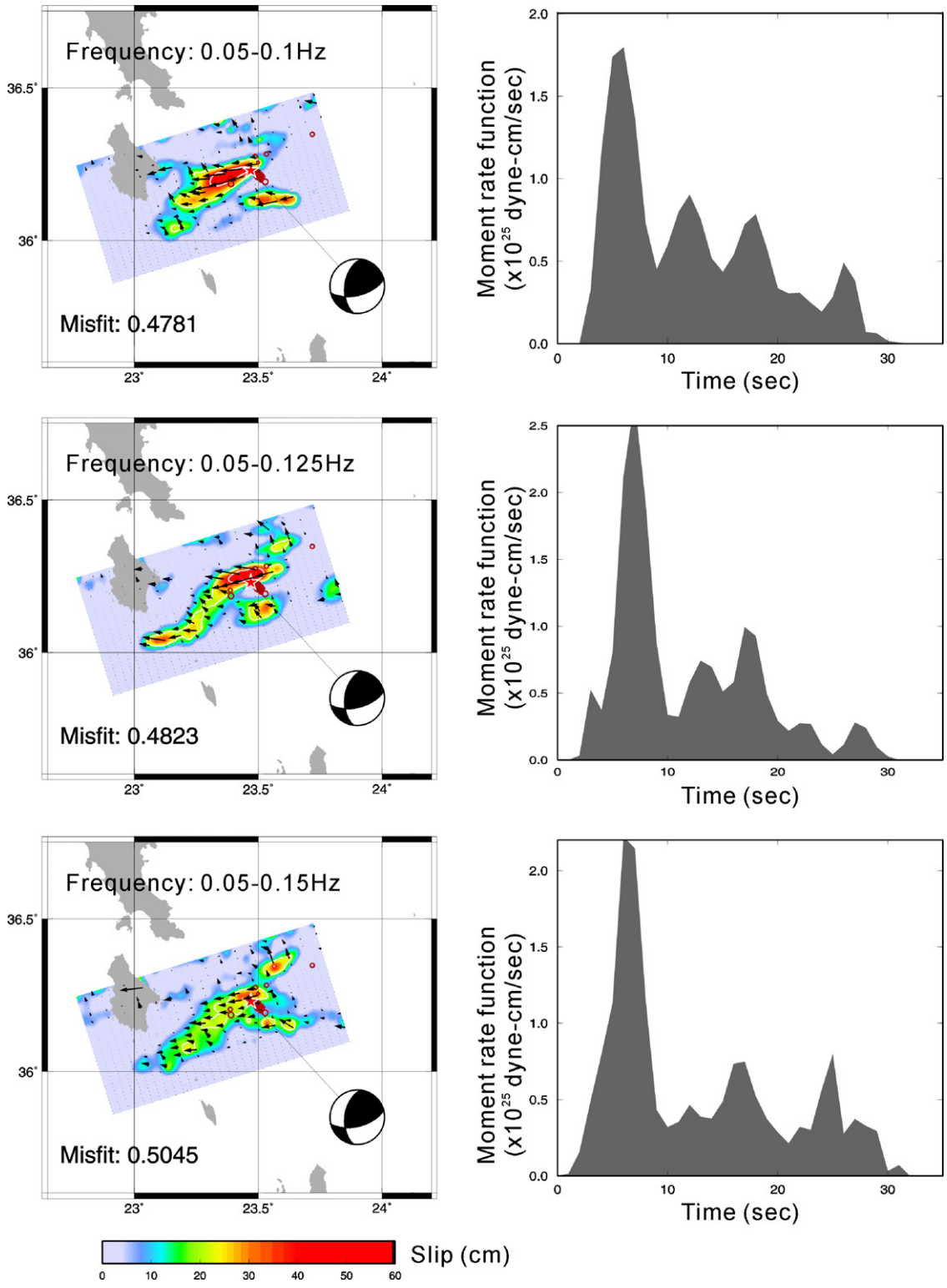


**Fig. 9.** Slip distribution and moment rate functions stemming from the inversion at three different frequency bands. Symbols plotted are the same as in Fig. 6.

35 km near the Hellenic trench to 120 km in the central Aegean, deepening further in the north to 220 km; (b) LAB in the area of southern and central Aegean that starts at 125 km and deepens to 200 km in northern Greece; (c) a slab thickness of 60–65 km. Moho depth estimates for the Aegean upper plate showed crustal thickness between 20 and 22 km for the Cretan Sea, 25–28 km for the Peloponnese and 25–33 km for Crete island in agreement with previous studies.

Fig. 13 shows a reconstruction of the descending slab geometry based on the aforementioned results, along a hypothetical profile that extends from the Hellenic trench to the central Aegean Sea. In the area of the Kythira strait the Aegean plate Moho is at 26–30 km depth, while the African slab Moho and LAB depth are located at 60 and 115 km, respectively. The Kythira earthquake was relocated at a hypocentral depth of about 51 km and is placed inside the slab, but close to the plate interface. Our slip inversion results show that

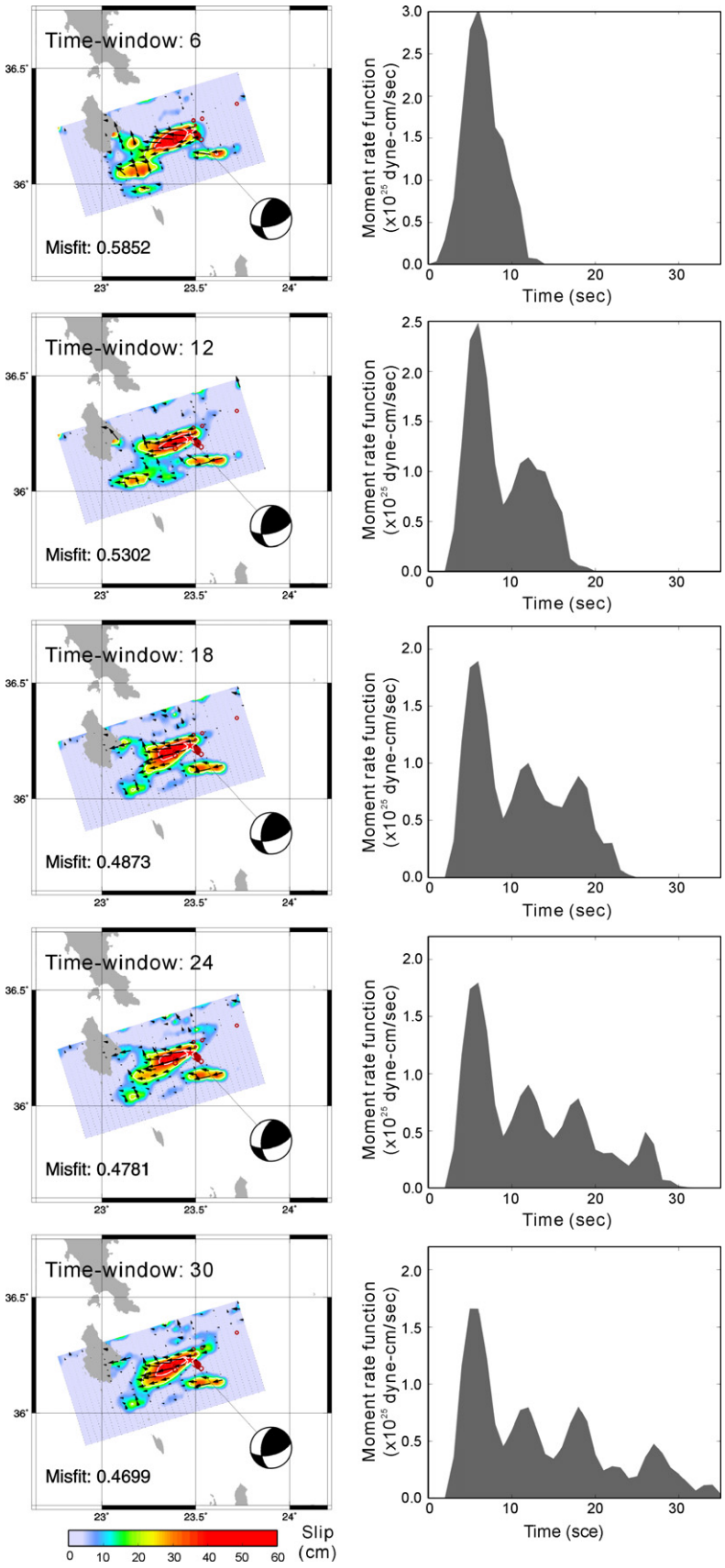


**Fig. 10.** Slip distribution and moment rate functions stemming from inversions using a different number of time windows. Symbols plotted are the same as in Fig. 6.

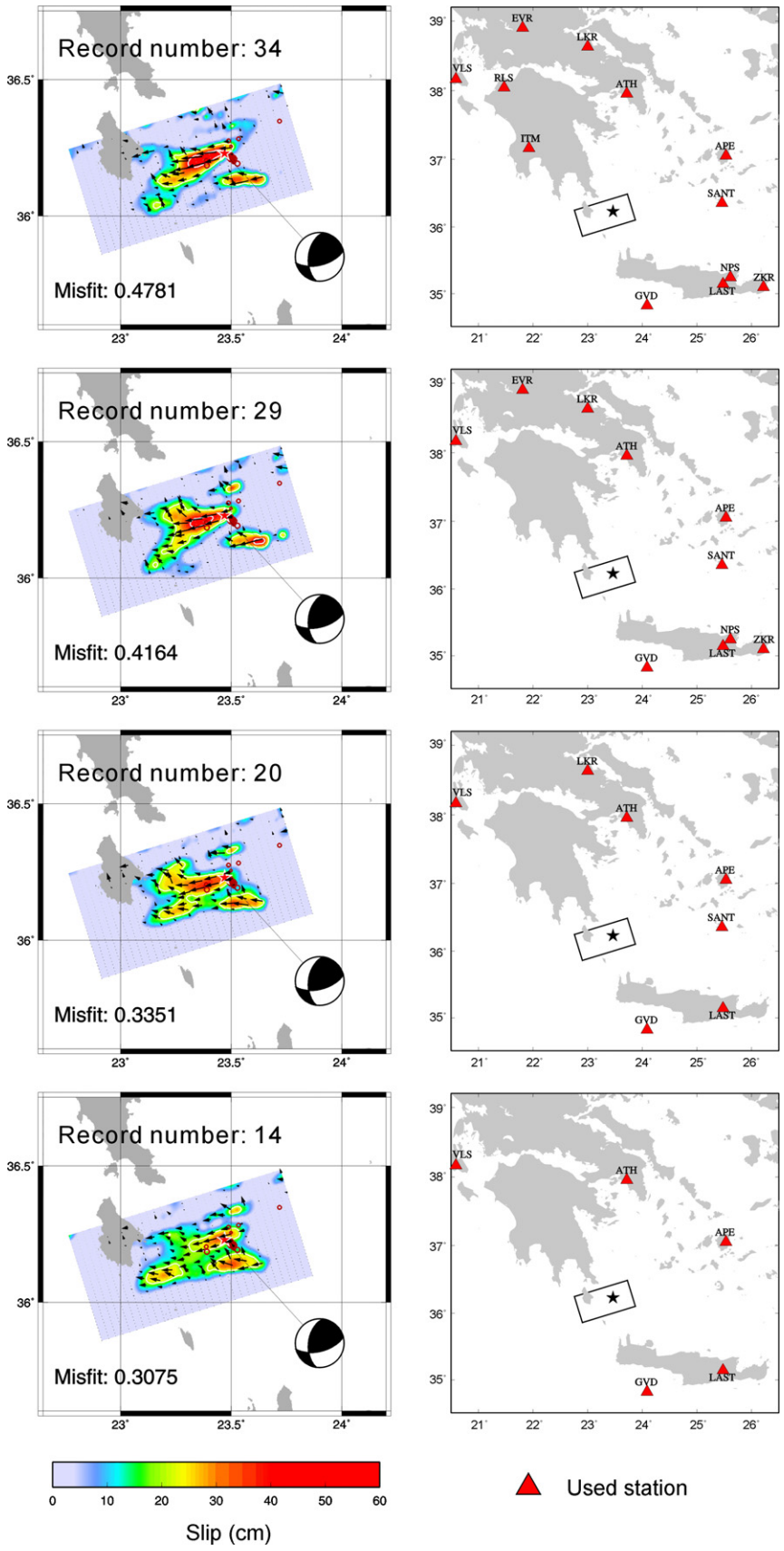


**Fig. 11.** Results of slip inversions using a different number of stations each time. Symbols plotted are the same as in Fig. 6. The maps in the right panel show the azimuthal distribution of used stations with respect to the Kythira event location.

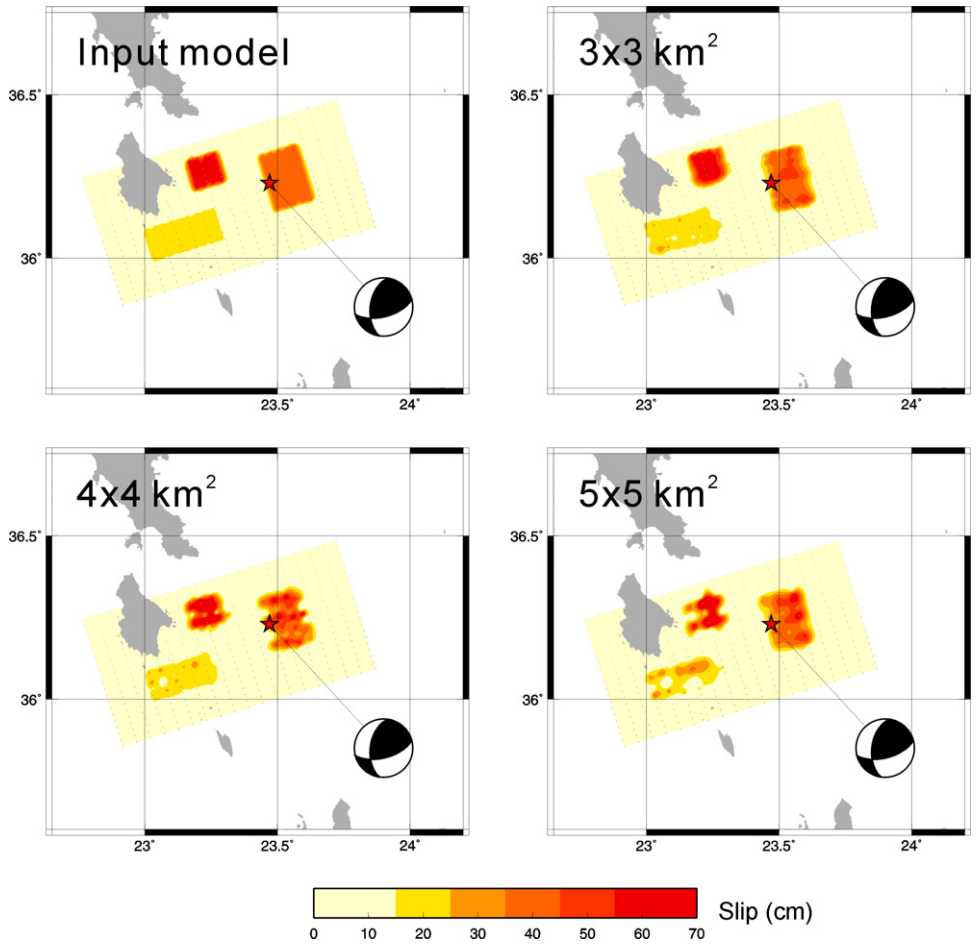


**Fig. 12.** Resolution test performed assuming the slip distribution model shown at the top left map. Results are presented as a function of subfault dimensions. All other parameters are the same as in the preferred slip distribution shown in Fig. 6.

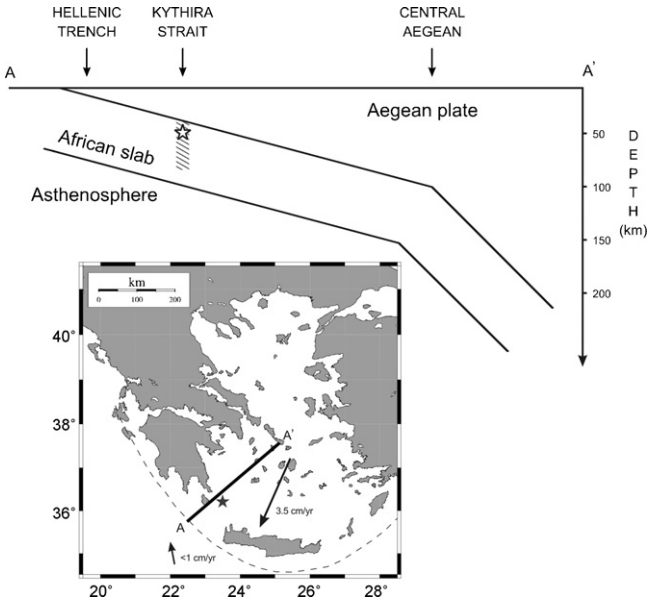


**Fig. 13.** Cartoon illustrating the subduction geometry of the African slab beneath the Aegean plate in a cross-section (see text for details). The star represents the hypocenter of the Kythira earthquake and the hatched zone its down-dip rupture extent. The thick black line on the inset map indicates the orientation of the cross-section and the arrows show the relative motion of the two plates after McClusky et al. (2000).

the rupture extends from a depth of about 40 km down to 80 km suggesting that the Kythira event ruptured most of the elastic part of the African lithosphere.

Well-located seismicity prior to the Kythira event (1964–2005), obtained from the global relocation database of Engdahl et al. (1998), shows that subcrustal (>30 km) earthquake activity decreases eastwards of the Hellenic trench (Fig. 14). Available focal mechanisms for this area reported by the Harvard or ETH groups can be divided into two categories based on their characteristics. Events with a focal depth shallower than 48 km exhibit mainly thrust faulting with nodal planes orientated parallel to the trench and subhorizontal P-axes trending in a NNE direction (i.e., almost parallel to the plate motion). These events probably represent interplate earthquakes and define the seismic coupling zone of the two plates at depths 35–48 km. Such values are in agreement with estimates of seismic coupling depth along subduction zones worldwide (Tichelaar and Ruff, 1993). Events deeper than 48 km exhibit oblique thrust faulting, their nodal planes are perpendicular or obliquely orientated to the trench and their P-axes are subhorizontal trending in a NNW direction (i.e., along the strike of the slab).

The Kythira earthquake seems to be correlated with this latter category of events, implying a coherent stress field across the Kythira strait. This stress field is probably associated with the along-strike compression of the African slab observed by many authors previously (e.g., Hatzfeld et al., 1993; Kiratzi and Papazachos, 1995; Benetatos et al., 2004). In particular, Hatzfeld et al. (1993) examined the microseismicity related to subcrustal earthquakes along the

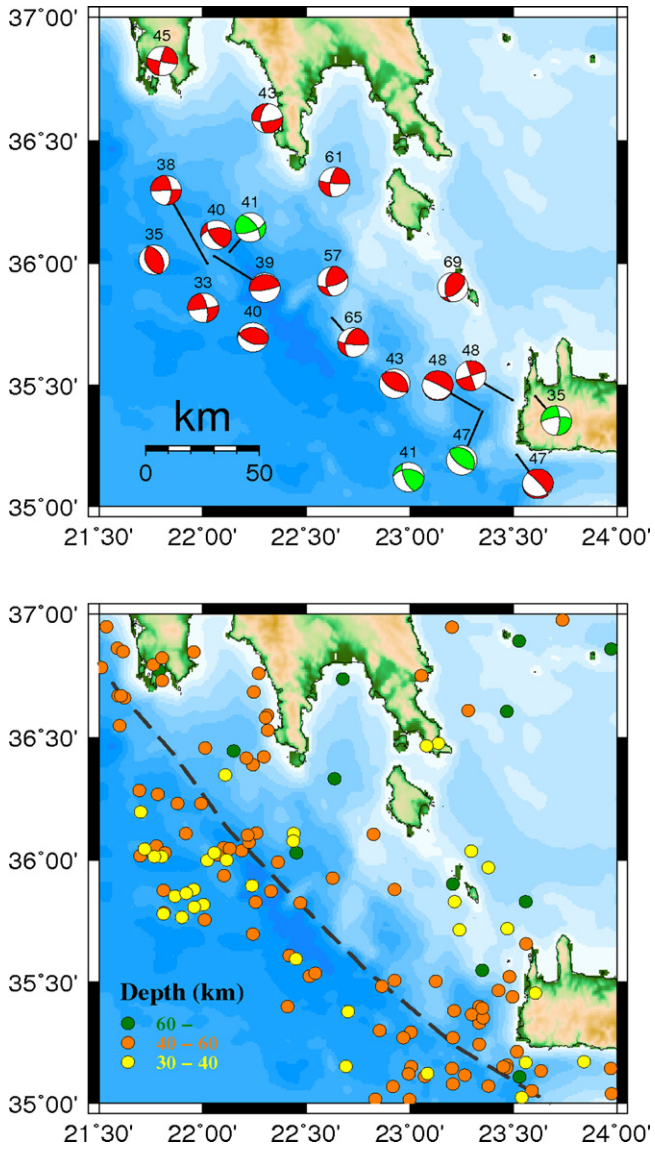


**Fig. 14.** Upper panel: map showing the distribution of available focal mechanisms of subcrustal events from the area of the Hellenic trench up to the Kythira strait. Red beach balls represent Harvard CMT solutions and green ones ETH solutions. The number on top of each beach ball is the hypocentral depth obtained from the relocation database of Engdahl et al. (1998). Lower panel: map showing well-located subcrustal seismicity for the period prior to the Kythira event (1964–2005) obtained from Engdahl et al. (1998). The depth of each event varies according to the scale given at the lower left hand corner. The trace of the Hellenic trench is plotted as a dashed black line. (For interpretation of the references to color in this figure legend, the reader is referred to the web version of the article.)

Hellenic arc. They suggested that the downgoing slab is markedly contorted and that its observed seismicity may reflect adjustments to this contortion. Such an interpretation also agrees well with the results of Knapmeyer and Harjes (2000), who observed an undulating topography of the African plate Moho beneath western Crete after analysis of migrated receiver functions. In this context, the area between western Crete and southern Peloponnese may represent the region where this contortion is expressed through the generation of events like the latest Kythira earthquake.

## 6. Conclusions

The main conclusions of this study can be summarized as follows:

1. The Kythira mainshock is relocated to the east of the Kythira island and at a hypocentral depth of 51 km, while its aftershocks form a tight cluster around it and are located at similar depths (44–53 km).
2. Finite fault inversion results confirm that the relocated source depth (51 km) for the Kythira event fits the data better than the initial depth estimate (65 km) and that the fault plane is the one dipping towards SE.
3. The slip distribution model of the Kythira earthquake consists of two patches of large slip, one located at depths 38–80 km and the other at 65–82 km effectively rupturing most of the elastic part of the African slab. The largest amount of moment was released during the first 11 s, while subsequent moment release probably accounts for coseismic slip on the surface of the fault.
4. The Kythira earthquake was probably caused by the contortion of the subducting African slab which results in the development of along-strike compression in the Kythira strait.

## Acknowledgments

This research was supported by the National Science Council of Taiwan through grants awarded to the first two authors (KIK, SJL). We are grateful to Jonathan Lees, an anonymous reviewer and the Editor George Helffrich, for their constructive criticism that helped to improve the original manuscript. N.S. Melis was partly supported by a NATO Collaborative Linkage Grant 979849.

## References

Ambraseys, N.N., 2001. Far-field effects of Eastern Mediterranean earthquakes in lower Egypt. J. Seismol. 5, 263–268.
Ambraseys, N.N., Adams, R.D., 1998. The Rhodes earthquake of 26 June 1926. J. Seismol. 2, 267–292.
Benetatos, C., Kiratzi, A., Papazachos, C., Karakaisis, G., 2004. Focal mechanisms of shallow and intermediate depth earthquakes along the Hellenic arc. J. Geodyn. 37, doi:10.1016/j.jog.2004.02.002.
Das, S., Henry, C., 2003. Spatial relation between main earthquake slip and its aftershock distribution. Rev. Geophys. 41, doi:10.1029/2002RG000119.
Dreger, D., 1994. Empirical Green's function study of the January 17, 1994 Northridge, California earthquake. Geophys. Res. Lett. 21, 2633–2636.
Endrun, B., Meier, T., Bischoff, M., Harjes, H.-P., 2004. Lithospheric structure in the area of Crete constrained by receiver functions and dispersion analysis of Rayleigh phase velocities. Geophys. J. Int. 158, doi:10.1111/j.1365-246X.2004.02332.x.
Engdahl, E.R., van der Hilst, R.D., Buland, R.P., 1998. Global teleseismic earthquake relocation with improved travel time and procedures for depth determination. Bull. Seism. Soc. Am. 88, 722–743.
Evangelidis, C.P., Konstantinou, K.I., Melis, N.S., Charalambakis, M., Stavrakakis, G.N., 2008. Waveform relocation and focal mechanism analysis of an earthquake swarm in Trichonis Lake, Western Greece. Bull. Seism. Soc. Am. 98, doi:10.1785/0120070185.
Hartzell, S.H., Heaton, T.H., 1983. Inversion of strong ground motion and teleseismic waveform data for the fault rupture history of the 1979 Imperial Valley, California earthquake. Bull. Seism. Soc. Am. 73, 1553–1583.
Hatzfeld, D., Martin, C., 1992. The Aegean intermediate seismicity defined by ISC data. Earth Planet. Sci. Lett. 113, 267–275.
Hatzfeld, D., Besnard, M., Makropoulos, K., Voulgaris, N., Kouskouna, V., Hatzidimitriou, P., Panagiotopoulos, P., Karakaisis, G., Deschamps, A., Lyon-Caen, H., 1993. Subcrustal microearthquake seismicity and fault plane solutions beneath the Hellenic arc. J. Geophys. Res. 98, 9861–9870.
Hutton, L.K., Boore, D.M., 1987. The ML scale in southern California. Bull. Seism. Soc. Am. 77, 2074–2094.
Karagianni, E.E., Papazachos, C.B., Panagiotopoulos, D.G., Suhaldoc, P., Vuan, A., Panza, G.F., 2005. Shear velocity structure in the Aegean area obtained by inversion of Rayleigh waves. Geophys. J. Int. 160, doi:10.1111/j.1365-246X.2005.02354.x.
Kiratzi, A., Papazachos, C.B., 1995. Active seismic deformation in the southern Aegean Benioff zone. J. Geodyn. 19, 65–78.
Klein, F., 2002. User's guide to Hypoinverse 2000, a FORTRAN program to solve for earthquake locations and magnitudes. USGS Open File Report 02-171.
Knapmeyer, M., Harjes, H.-P., 2000. Imaging crustal discontinuities and the downgoing slab beneath western Crete. Geophys. J. Int. 143, 1–21.
Konstantinou, K.I., Kalogeras, I.S., Melis, N.S., Kourouzidis, M.C., Stavrakakis, G.N., 2006. The 8 January 2006 earthquake (Mw 6.7) offshore Kythira island, southern Greece: Seismological, strong-motion and macroseismic observations of an intermediate-depth event. Seism. Res. Lett. 77, 544–553.
Konstantinou, K.I., Melis, N.S., 2008. High frequency shear wave propagation across the Hellenic subduction zone. Bull. Seism. Soc. Am. 98, doi:10.1785/0120060238.

Lay, T., Wallace, T.C., 1995. Modern Global Seismology. Academic Press, New York.
Lee, S.-J., Ma, K.-F., 2000. Rupture process of the 1999 Chi-Chi, Taiwan earthquake from the inversion of teleseismic data. Terr. Atmos. Ocean. Sci. 11, 591–608.
Lee, S.-J., Ma, K.-F., Chen, H.-W., 2006. Three-dimensional dense strong motion waveform inversion for the rupture process of the 1999 Chi-Chi Taiwan, earthquake. J. Geophys. Res. 111, B11308, doi:10.1029/2005JB004097.
Lin, G., Shearer, P.M., 2005. Tests of relative earthquake location techniques using synthetic data. J. Geophys. Res. 110, B04304, doi:10.1029/2004JB003380.
Lin, G., Shearer, P.M., 2006. The COMPLOC earthquake location package. Seism. Res. Lett. 77, 440–444.
Li, X., Bock, G., Vafidis, A., Kind, R., Harjes, H.-P., Hanka, W., Wylegalla, K., van der Meijde, M., Yuan, X., 2003. Receiver function study of the Hellenic subduction zone: imaging crustal thickness variations and the oceanic Moho of the descending African lithosphere. Geophys. J. Int. 155, 733–748.
Ma, K.-F., Mori, J., Lee, S.-J., Yu, S.B., 2001. Spatial and temporal distribution of slip for the 1999 Chi-Chi, Taiwan earthquake. Bull. Seism. Soc. Am. 91, 1069–1087.
McClusky, et al., 2000. Global positioning system constraints on plate kinematic and dynamics in the Eastern Mediterranean and Caucasus. J. Geophys. Res. 105, 5695–5719.
Melis, N.S., Konstantinou, K.I., 2006. Real-time seismic monitoring in the Greek region: an example from the 17 October 2005 East Aegean Sea earthquake sequence. Seism. Res. Lett. 77, 364–370.
Novotny, O., Zahradnik, J., Tselentis, G.-A., 2001. Northwestern Turkey earthquakes and the crustal structure inferred from surface waves observed in western Greece. Bull. Seism. Soc. Am. 91, 875–879.
Nyst, M., Thatcher, W., 2004. New constraints on the active tectonic deformation of the Aegean. J. Geophys. Res. 109, B11406, doi:10.1029/2003JB002830.
Papazachos, C.B., Nolet, G., 1997. P and S velocity structure of the Hellenic area obtained by robust nonlinear inversion of travel times. J. Geophys. Res. 102, 8349–8367.
Papazachos, B.C., Papazachou, K., 1997. The earthquakes of Greece, Ziti edition. Thessaloniki.
Papazachos, B.C., Karakostas, V.G., Papazachos, C.B., Scordilis, E.M., 2000. The geometry of the Wadati–Benioff zone and lithospheric kinematics in the Hellenic arc. Tectonophysics 319, 275–300.
Richards-Dinger, K.B., Shearer, P.M., 2000. Earthquake locations in southern California obtained from source-specific station terms. J. Geophys. Res. 105, 10939–10960.
Shearer, P.M., 1997. Improving local earthquake locations using the L1 norm and waveform cross-correlation: application to the Whittier Narrows, California aftershock sequence. J. Geophys. Res. 102, 8269–8283.
Sodoudi, F., Kind, R., Hatzfeld, D., Priestley, K., Hanka, W., Wylegalla, K., Stavrakakis, G., Vafidis, A., Harjes, H.-P., Bohnhoff, M., 2006. Lithospheric structure of the Aegean obtained from P and S receiver functions. J. Geophys. Res. 111, B12307, doi:10.1029/2005JB003932.
Spakman, W., Wortel, M.J.R., Vlaar, N.J., 1988. The Hellenic subduction zone: a tomographic image and its geodynamic implications. Geophys. Res. Lett. 15, 60–63.
Tichelaar, B.W., Ruff, L.J., 1993. Depth of seismic coupling along subduction zones. J. Geophys. Res. 98, 2017–2037.